RSC Advances

PAPER

View Article Online
View Journal | View Issue

Cite this: *RSC Adv.*, 2023, **13**, 21861

MIL-88B(Fe)-NH_2: an amine-functionalized metal–organic framework for application in a sensitive electrochemical sensor for Cd^{2+}, Pb^{2+}, and Cu^{2+} ion detection†

Luyen T. Tran, Hue T. M. Dang,* Hoang V. Tran,* Giang T. L. Hoang and Chinh D. Huynh

We propose here an electrochemical platform for multi-heavy metal ion detection in water based on MIL-88B(Fe)-NH_2, an amine-functioned metal–organic framework (MOF) for modifying the surface of a glassy carbon electrode (GCE). Herein, MIL-88B(Fe)-NH_2 with abundant functionalized amine groups can play the role of capture sites for the enrichment of metal ions before electrochemical oxidation sensing. MIL-88B(Fe)-NH_2 was synthesized under optimized conditions through a solvothermal method and characterized by X-ray diffraction (XRD), scanning electron microscopy (SEM), transition electron microscopy (TEM), Fourier-transform infrared spectroscopy (FT-IR), cyclic voltammetry (CV) and electrochemical impedance spectroscopy (EIS) techniques. MIL-88B(Fe)-NH_2 was then drop-casted on GCE to electrochemically determine the Cd^{2+}, Pb^{2+} and Cu^{2+} ion concentrations by differential pulse voltammetry (DPV). The electrochemical sensor exhibits excellent electrochemical performance toward Cd^{2+}, Pb^{2+} and Cu^{2+} ions in the large linear ranges of 0.025–1.000 μM, 0.3–10.0 μM and 0.6–10.0 μM with limits of detection that are 2.0×10^{-10} M, 1.92×10^{-7} M and 3.81×10^{-7} M, respectively. The fabricated sensor also shows high reliability and good selectivity. This MIL-88B(Fe)-NH_2 application strategy is promising for the evaluation of various heavy metal ions in water.

Received 29th April 2023
Accepted 6th July 2023

DOI: 10.1039/d3ra02828c

rsc.li/rsc-advances

1. Introduction

Metal–organic framework (MOF) is a unique class of porous materials constituting metal ions (or clusters) and organic ligands that link together *via* coordination bonds. Due to their unique structure, MOFs have high specific porosity and surface area,[1,2] tunable chemical functionalization, reversible adsorption, and high catalytic ability.[3] As a result, MOFs can be applied in various fields, such as gas storage and separation,[4,5] drug delivery,[6,7] chemical separation,[8] catalysis,[9] cell imaging,[10] and sensing.[11–13] In terms of the sensing domain, MOFs are considered as a promising material class for the detection of various contaminants, such as organic substances,[14,15] antibiotics,[16–19] inorganic and heavy metal ions,[20] owing to good physicochemical properties (*e.g.*, large surface area, sensitivity to target ions, and versatile structure). For the synthesis of MOFs materials, linear organic linkers, such as terephtalic acid, have been widely used due to their ability to create open framework structures. The presence of functional groups in the organic linkers leads to changes in the physicochemical behavior of the MOFs products, including the Brønsted/Lewis acid/base properties, the solubility of the starting materials, and the changes in the pore opening (flexibility) and in the adsorption selectivity to targets.[21–23] On the organic linker molecule, the amino groups (–NH_2) have lone pair electrons and act as the Lewis base. They can form coordinate bonds with the heavy metal ions. Thus, using NH_2-functionalized MOFs as sensors to detect heavy metals is significant. In this study, we chose 2-aminoterephtalic acid (H_2N-BDC), which is the one of the simplest amino diacids as an organic linker for the synthesis of MIL-88B(Fe)-NH_2 (MIL: Materials of Institute Lavoisier), a common MOF whose structure is built up by Fe^{3+} clusters and 2-aminoterephthalate anionic ligands.[24] The outstanding advantages of MIL-88B(Fe)-NH_2 compared to other MOFs are its chemical stability, less toxicity, and abundant raw sources. Thus, it attracts considerable research in different applications including adsorption, sodium-ion batteries, and heterogeneous catalysis.[25–29] However, the use of MIL-88B(Fe)-NH_2 in the fabrication of electrochemical sensors for the detection of heavy metal ions is a relatively new issue that requires further investigation.

Nowadays, the term "heavy metal" has been utilized to describe metallic elements that are harmful to the environment and humans. In recent decades, heavy metal pollution has

School of Chemical Engineering, Hanoi University of Science and Technology, 1 Dai Co Viet Road, Hai Ba Trung District, Hanoi 100000, Vietnam. E-mail: hue.dangthiminh@hust.edu.vn; hoang.tranvinh@hust.edu.vn

† Electronic supplementary information (ESI) available. See DOI: https://doi.org/10.1039/d3ra02828c

become increasingly serious due to global population growth and industrial development. Transportation, farming activities, and industrial manufacturing like pesticides, metallurgy, oil refining, and chemicals have released an excessive amount of heavy metal (ions) into the environment. These contaminants cannot be degraded or demolished, leading to accumulation in the environment and the consequent contamination of food chains—a severe threat to human health and species. For instance, people who consume large quantities or get regularly exposed to cadmium (Cd) have a higher rate of prostate and lung cancers than others.[30] Furthermore, lead (Pb) is harmful to the digestive, cardiovascular, nervous, and kidney systems.[31] Another example is copper (Cu), an essential trace metal for some biological functions. However, at elevated concentrations, it can destroy many red blood cells, or result in neurological symptoms, including behavioral abnormalities, tremors of the hands, unclear speech, and others.[32] Thus, examining the concentration of the heavy metal (ions) is urgent and essential.

Among many methods used to detect heavy metal ions in the water environment, MOF-based sensors show great potential for application in practice by the possibility to build portable instruments, its high sensitivity, and the ability obtain quick results.[20] MOF-based sensors for heavy metal ion sensing are classified into optical sensors[33,34] and electrochemical sensors.[20,35–40] Furthermore, electrochemical sensors with its many advantages, such as high sensitivity and selectivity, wide linear response range, good stability and reproducibility, quick detection, ease of use, and reasonable cost, have many potential applications for the monitoring of heavy metal ions.[20,36]

In this work, the metal–organic framework MIL-88B(Fe)-NH_2 was synthesized. The specific characteristics of the obtained MIL-88B(Fe)-NH_2 samples were investigated using a number of chemical-physical techniques in order to select the optimized synthesis conditions. Then, the MIL-88B(Fe)-NH_2 material was used to modify the glassy carbon electrode (GCE) to develop the sensitive electrochemical sensor for the detection of Cd^{2+}, Pb^{2+}, and Cu^{2+} ions in aqueous solutions.

2. Experimental

2.1. Chemicals and instrumentation

2-Aminoterephthalic acid H_2N-C_6H_3-1,4-$(COOH)_2$ (NH_2-TPA) (99 wt%), iron(III) chloride hexahydrate $FeCl_3 \cdot 6H_2O$ (99 wt%), methanol CH_3OH (MeOH) (anhydrous, 99.8 v/v%), sodium acetate CH_3COONa (99 wt%), acetic acid CH_3COOH (99.5 wt%), cadmium nitrate tetrahydrate $Cd(NO_3)_2 \cdot 4H_2O$ (99 wt%), lead nitrate $Pb(NO_3)_2$ (99 wt%), and copper sulfate pentahydrate $CuSO_4 \cdot 5H_2O$ (99 wt%.) were purchased from Sigma-Aldrich. Cobalt sulphate heptahydrate ($CoSO_4 \cdot 7H_2O$ 99.5 wt%), nickel sulphate hexahydrate ($NiSO_4 \cdot 6H_2O$ 98.5 wt%), potassium dichromate ($K_2Cr_2O_7$ 99.8 wt%), and zinc chloride ($ZnCl_2$ 98 wt%.) were supplied by Xilong Chemical Co., China. The appropriate amounts of sodium acetate and acetic acid were used to prepare acetate buffer solution 0.1 M (ABS) with pH 6.0. Dimethylformamide C_3H_7NO (DMF) (99.94 v/v%) was purchased from Fisher Chemical. Polyethylene glycol 2000 ($H(OCH_2CH_2)_nOH$, PEG 2000) was supplied by Alfa Aesar.

A Siemens D5005 diffractometer (Cu K_α radiation, λ = 1.54056 Å), a NICOLET iS50FT-IR spectrometer, a Hitachi S4800 scanning electron microscope (SEM), and a TECNAI F20-G2 high-resolution transmission electron microscope (TEM) were used to perform X-ray diffraction (XRD), Fourier-transform infrared spectroscopy (FT-IR), SEM, and TEM measurements, respectively. Electrochemical measurements were conducted using a PGSTAT302N AutoLab electrochemical workstation (Metrohm, Netherlands).

2.2. Optimization of the synthetic conditions of MIL-88B(Fe)-NH_2

Fig. 1 shows a typical process for the synthesis of MIL-88B(Fe)-NH_2 by the solvothermal method. To investigate the impact of the molar ratio between the metal ion and the ligand on the formation of MIL-88B(Fe)-NH_2, 1.15 mmol $FeCl_3$ and 1.15x (mmol) H_2N-C_6H_3-1,4-$(COOH)_2$ (wherein, x = 1.0; 1.2; 1.5 and 2.0, respectively) were mixed into 25 mL of DMF solvent using a magnetic stirrer until homogeneous solutions were obtained. The solutions were added into autoclaves, and then the reactions were performed hydrothermally at 150 °C. The obtained powder products were separately washed by DMF, methanol and distilled water, and were subsequently dispersed into distilled water overnight. The MIL-88B(Fe)-NH_2(x) materials were obtained by centrifuging and vacuum-drying at 170 °C within 12 hours. The same experiments were carried out to study the effect of the hydrothermal time on the crystalline phase formation of MIL-88B(Fe)-NH_2 at different periods, including 8, 12, 18, and 24 hours.

2.3. MIL-88B(Fe)-NH_2 modification of a glassy carbon electrode

Firstly, glassy carbon electrodes (GCE) were polished by 1 μm Al_2O_3 slurry on polishing cloth, and then washed with water and ethanol. A total of 3.0 mg of MIL-88B(Fe)-NH_2 and 3.0 mg of PEG-2000 were dispersed into 1 mL of deionized water using ultrasonication for 10 minutes. Then, 5 μL of this solution was dropped onto a freshly polished GCE, and dried in air to obtain the MIL-88B(Fe)-NH_2 modified GCE (GCE/MIL-88B(Fe)-NH_2).

2.4. Electrochemical measurements and electrochemical sensing of Cd^{2+}, Pb^{2+}, and Cu^{2+} ions

The three-electrode configuration consists of the GCE/MIL-88B(Fe)-NH_2 as the working electrode (WE), a Pt wire as the counter electrode (CE), and Ag/AgCl as the reference electrode (RE). Cyclic voltammetry (CV) and electrochemical impedance spectroscopy (EIS) measurements of the GCE and the GCE/MOFs in a solution containing 0.005 M $K_3[Fe(CN)_6]$, 0.005 M $K_4[Fe(CN)_6]$, and 0.1 M KCl were performed. CVs were studied at a scan rate of 25 mV s^{-1}. EIS spectra were recorded in a frequency range from 100 kHz to 0.1 Hz, E_{AC} = 5 mV, and E_{DC} = 160 mV. The fabricated GCE/MOFs sensor was used to detect cadmium, lead and copper ions (in ABS) using DPV measurements with a deposition potential of −1.2 V, a deposition time of 120 seconds, a pulse amplitude of 50 mV, a pulse width of 50

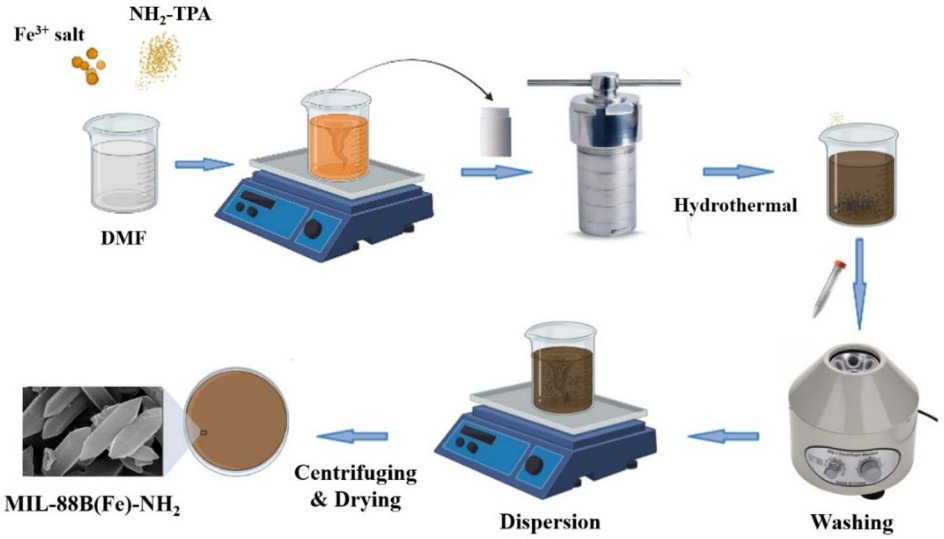

Fig. 1 Depiction of the MIL-88B(Fe)-NH_2 synthesis.

ms, a desorption potential of 0.4 V, and a desorption time of 60 seconds.

3. Results and discussion

3.1. Characterization of MIL-88B(Fe)-NH_2

3.1.1 X-ray diffraction (XRD) patterns. XRD patterns of the obtained MIL-88B(Fe)-NH_2 with the various x values (herein, x is the molar ratios of H_2N-C_6H_3-1,4-$(COOH)_2$/Fe(III) ions) are displayed in Fig. 2A. In particular, when $x = 1.0$ (line a) and 1.2 (line b), the formation of the MIL-88B(Fe)-NH_2 phase is observed, which are characterized by $2\theta \approx 9.3°$ and 10.6°, corresponding to the (002) and (101) lattice faces, respectively (CCDC 647646). However, the γ-Fe_2O_3 crystalline phase also appears at $2\theta \approx 25.0°$ and 29.0° (JCPDS 39-1346), which is caused by a residual amount of Fe(III) ions. At higher proportions with $x = 1.5$ (line c) and $x = 2.0$ (line d), the XRD pattern only shows the typical peaks of the MIL-88B(Fe)-NH_2 crystal. These characteristic peaks are very clear and sharp, indicating that the MIL-88B(Fe)-NH_2 crystals are completely formed. The average crystal size of the MIL-88B(Fe)-NH_2 is calculated by Scherrer formula for the lattice of (101):

$$D = \frac{0,9\lambda}{\beta_{hkl}\cos\theta} \quad (1)$$

where D is the average particle size in nm, k is the constant depending on the crystallite shape (0.9), λ is the wavelength of the copper K_α X-ray radiation, β is the FWHM of the most intense peak (in rad), and θ is the diffraction angle. The average crystallite size can be estimated around 22.8 and 23.3 nm for MIL-88B(Fe)-NH_2($x = 1.5$) and MIL-88B(Fe)-NH_2($x = 2.0$) samples, respectively. Fig. 2B manifests the XRD patterns of the MIL-88B(Fe)-NH_2(1.5) material at the different hydrothermal periods. The sample that performed for 8 hours forms the material phase, but the diffraction peaks of γ-Fe_2O_3 still exist. With the periods of 12, 18 and 24 hours, the characteristic peaks of MIL-88B(Fe)-NH_2 appear and do not have any peaks of other materials, proving the purified phase of the MIL-88B(Fe)-NH_2. The calculated crystallinities of the materials are 86.80, 79.97 and 70.28% for the 12, 18 and 24 hours samples, respectively. It can be seen that increasing the reaction time causes a detrimental effect on the material's crystallinity. Recrystallization occurs under high temperature and pressure conditions, leading to the crystallinity reduction.[41] Similar degradation phenomena have been observed in several other MOFs.[42,43] Based on these findings, the MIL-88B(Fe)-NH_2 sample synthesized at $x = 1.5$ and hydrothermal treatment for 12 hours was selected for further investigations of the electrochemical behaviors and applications for electrochemical sensor developments.

3.1.2 FT-IR spectra. Fig. 2C shows the FT-IR spectra of the TPA-NH_2 ligand (curve a), MIL-88B(Fe)-NH_2(1.5) (curve b) and MIL-88B(Fe)-NH_2(2.0) (curve c). Namely, a peak appears at 3454 cm^{-1} owing to the stretching oscillation of the N–H bonds. The peaks at 1578 cm^{-1} and 1379 cm^{-1} are attributed to the presence of the C–O asymmetric and symmetric stretching oscillations, respectively. Another peak obtained at 1620 cm^{-1} represents a carbonyl group (C=O), but the peak is not clear due to the strong intensity of the C–O peak. The peaks at 1254 cm^{-1} and 769 cm^{-1} correspond to the bending vibration of the C sp^2–N and C sp^2–H bonds, respectively. The above features are observed in the spectra of the TPA-NH_2 ligand and synthesized materials. Specially, the characteristic peak at 554 cm^{-1} (FeO) appears in the MOF's patterns, which represents the coordination bond between Fe^{3+} and the ligand. As such, FT-IR spectroscopy contributes to confirming the formation of the bond between Fe(III) and the ligand *via* the oxygen atom in the synthesized MOFs.

3.1.3 BET analysis. The evaluated BET surface area of the synthesized MIL-88B(Fe)-NH_2(1.5) is 13.43 $m^2\ g^{-1}$. This value is consistent with previous studies (Table 1),[44–46] and the BET area of MIL-88B(Fe)-NH_2(1.5) is still higher than that of other

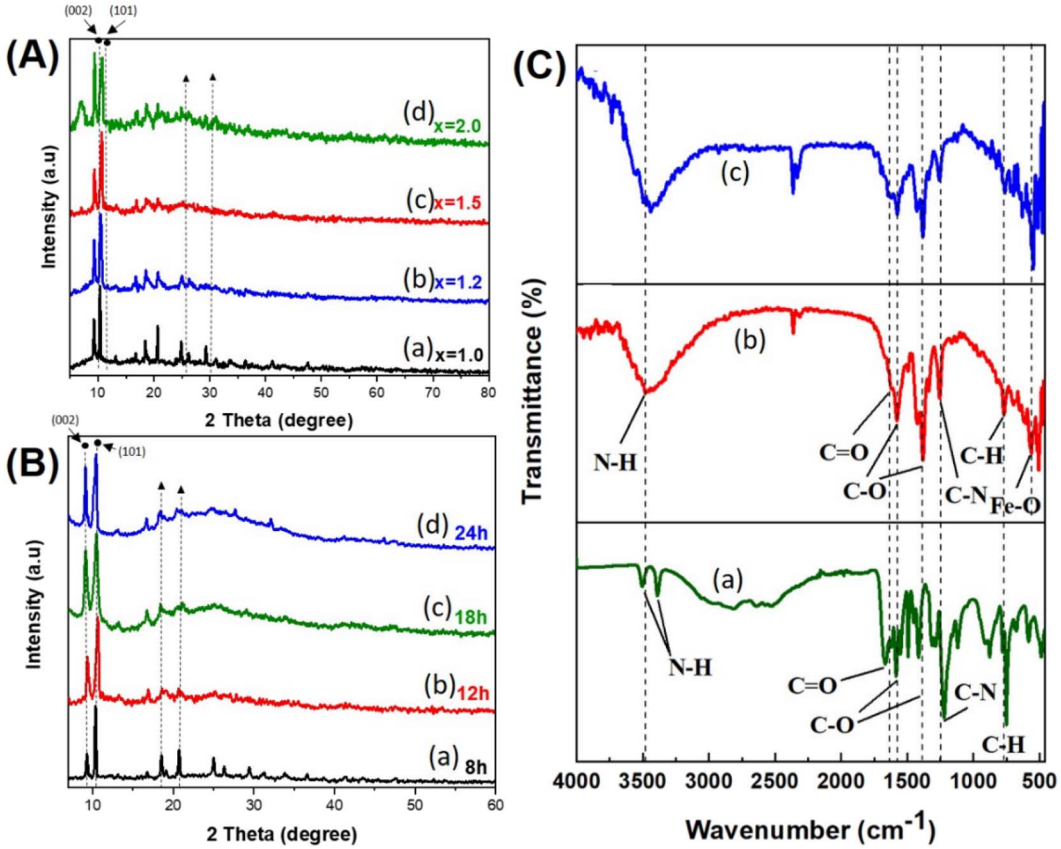

Fig. 2 (A and B) XRD patterns of the synthesized MIL-88B(Fe)-NH_2 materials (A) with different molar ratios of H_2N-C_6H_4-1,4-$(COOH)_2$/Fe^{III}; (B) at different hydrothermal temperatures; and (C) FT-IR spectra of (a) TPA-NH_2, (b) MIL-88B(Fe)-NH_2(1.5) and (c) MIL-88B(Fe)-NH_2(2.0).

Table 1 Specific surface area of some MIL-88BNH_2

Materials	S_{BET} (m^2 g^{-1})	References
MIL-88B(Fe)-NH_2	19.2	44
MIL-88B(Fe)-NH_2	2.35	45
MIL-88B(Fe)-NH_2	8.9	46
MIL-88B(Fe)-NH_2	13.43	This study

reported MIL-88B(Fe)-NH_2 and Fe-MOFs materials.[45–47] The causes can be attributed to the synthesis method and more importantly, to the closed microporous structures of MIL-88B(Fe)-NH_2. Furthermore, some Fe-MOFs are not sensitive to nitrogen gas because the nitrogen molecule's size and the pore's size of these MOFs materials are comparable.[44–48]

3.1.4 SEM and TEM images. The MIL-88B(Fe)-NH_2 morphologies at the ratios of 1.5 and 2.0 were characterized by SEM and TEM, as shown in Fig. 3. The SEM images exhibit a uniform distribution of the material particles, whose size distribution and average size were calculated using ImageJ software. The mean widths of MIL-88B(Fe)-NH_2(1.5) and MIL-88B(Fe)-NH_2(2.0) are 414.3 and 377.5 nm, respectively; corresponding to the mean length/width ratio of 3.97 and 3.81 (inserted figures in Fig. 3D and H, respectively; and Table S1†). Although the size tends to decrease with increasing molar ratio, no morphological change is observed. This is also clearly shown in the TEM images (Fig. 3C–F), where the particle sharpness at the two ratios is similar.

3.2. Electrochemical characteristics of the fabricated MIL-88B(Fe)-NH_2

Fig. 4 gives the CV (Fig. 4A) curves and the EIS spectra (Fig. 4B) recorded in a solution containing 0.005 M $K_3Fe(CN)_6$, 0.005 M $K_4Fe(CN)_6$, and 0.1 M KCl of the GCE (curve a) and the GCE/MIL-88B(Fe)-NH_2 (curve b), respectively. It can be seen in Fig. 4A that in the case of the GCE/MIL-88B(Fe)-NH_2 (curve b), the anodic and cathodic peak currents are higher than that of the GCE (curve a), indicating an increase in the electroactive area due to the modification of the GCE with MIL-88B(Fe)-NH_2. As shown in Fig. 4B, the EIS spectra of the two electrodes have a semicircle characterizing a charge transfer process and a linear region characterizing a diffusion process. An equivalent circuit (Fig. 4B, inset), which includes a solution resistance (R_s), a charge transfer resistance (R_{ct}), a constant phase element (Q_{CPE}), and a Warburg diffusion coefficient (W), can be used to simulate the EIS spectra, and the corresponding fitted plots are shown in Fig. 4B (curve (a′) and curve (b′)). The fitted R_{ct} results of the GCE and the GCE/MIL-88B(Fe)-NH_2 are 4377 Ω and 3440 Ω, respectively. Thus, the electrochemical performances demonstrate that the MIL-88B(Fe)-NH_2 layer drop-casted on GCE is able to remarkably enhance the electrochemical signal of GCE/MIL-88B(Fe)-NH_2.

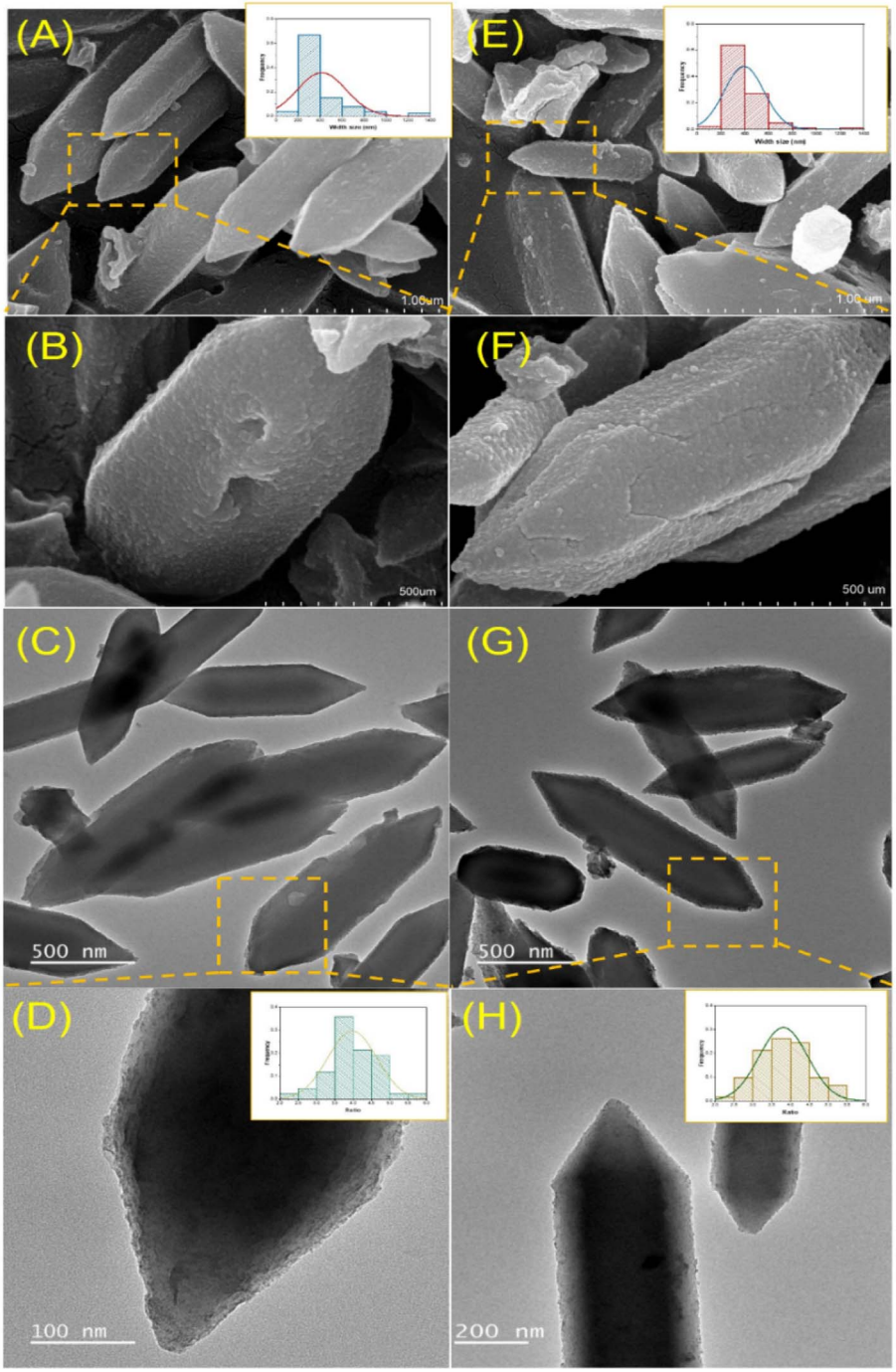

Fig. 3 (A–D) SEM and (E–H) TEM images of (A–D) MIL-88B(Fe)-NH_2(1.5), (E–H) MIL-88B(Fe)-NH_2(2.0). Inserted figures: (A and E) the width size distribution and (D and H) the ratio of the length to the width of (A and D) MIL-88B(Fe)-NH_2(1.5) and (E and H) MIL-88B(Fe)-NH_2(2.0).

3.3. Electrochemical detection of Cd^{2+}, Pb^{2+}, and Cu^{2+} ions using GCE/MIL-88B(Fe)-NH_2

DPV measurements of the GCE and the GCE/MIL-88B(Fe)-NH_2 were performed in a solution containing 20 μM Cd^{2+}, 20 μM Pb^{2+}, 20 μM Cu^{2+} and 0.1 M ABS (pH = 6.0), in order to investigate the ability of using the GCE/MIL-88B(Fe)-NH_2 as an electrochemical sensor for the detection of Cd^{2+}, Pb^{2+}, and Cu^{2+} ions in aqueous solutions, and the obtained results are described in Fig. 5. It can be clearly seen in Fig. 5 (curve a) that with regards to GCE, there are no peaks. In contrast, in Fig. 5 (curve b), with regards to GCE/MIL-88B(Fe)-NH_2, there are three peaks at −0.79 V, −0.52 V, and −0.02 V, which are associated with the presence of Cd^{2+}, Pb^{2+}, and Cu^{2+} ions, respectively.[49] The results indicate that the GCE modified with MIL-88B(Fe)-NH_2 can be used as an electrochemical sensor for the determination of Cd^{2+}, Pb^{2+}, and Cu^{2+} ions in aqueous solutions.

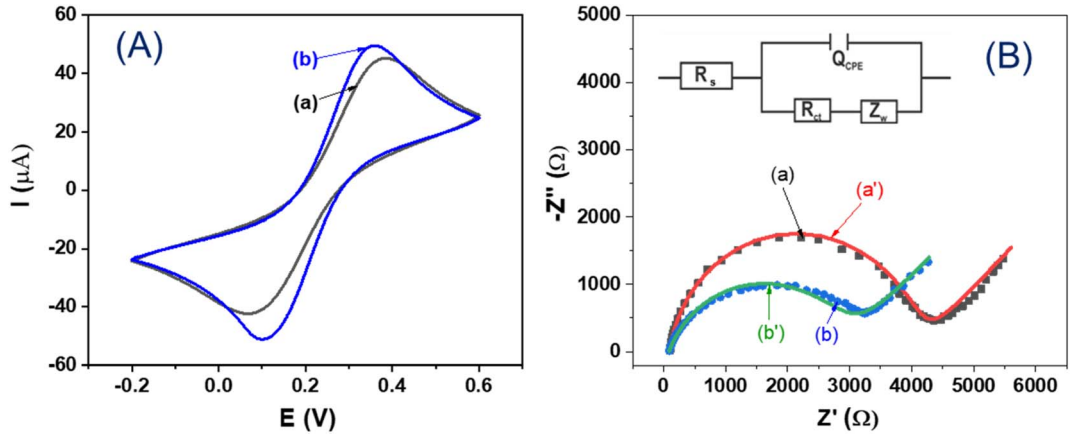

Fig. 4 (A) CV scans and (B) EIS spectra (Nyquist plots) of (a) GCE and (b) GCE/MIL-88B(Fe)-NH_2; (inserted figure in (B): Randles equivalent circuit; (a′) and (b′): corresponding fitted plots). Experimental conditions: 0.1 M KCl solution containing $K_3Fe(CN)_6/K_4Fe(CN)_6$ (0.005 M) as the electrolyte. CVs were measured at a scan rate of 25 mV s^{-1}. EIS spectra were recorded with a frequency range from 100 kHz to 0.1 Hz, $E_{AC} = 5$ mV, and $E_{DC} = 160$ mV.

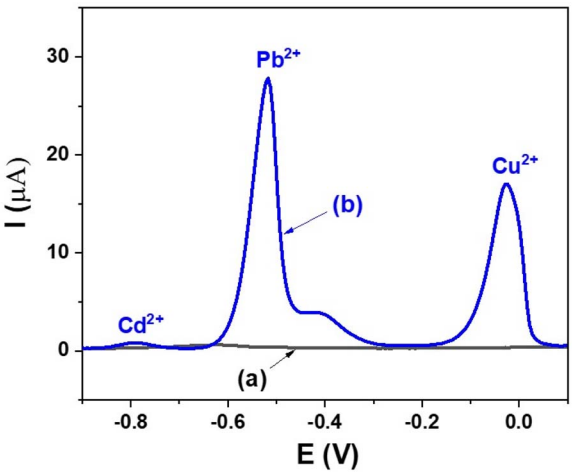

Fig. 5 DPV results of (a) GCE and (b) GCE/MIL-88B(Fe)-NH_2 measured in a solution containing 20 μM Cd^{2+}, 20 μM Pb^{2+}, 20 μM Cu^{2+} and 0.1 M ABS (pH = 6.0).

DPV measurements of the GCE/MIL-88B(Fe)-NH_2 electrodes were performed in 0.1 M ABS (pH = 6.0) solutions containing 10 μM Cd^{2+}, 10 μM Pb^{2+}, and 10 μM Cu^{2+} with differential measuring conditions, including potential step, pulse width, and pulse amplitude, in order to investigate the optimization studies for DPV, and the obtained results are described in Fig. 1S (A, B, and C, respectively).† As can be seen in Fig. 1S(A, B, and C),† when the potential step is 5 mV, the pulse width is 50 ms, and the pulse amplitude is 50 mV, the obtained DPV signal is the best for Cd^{2+}, Pb^{2+}, and Cu^{2+}. Therefore, in this work, these measuring conditions were selected for DPV measurements.

Fig. 6A provides the DPV results of the GCE/MIL-88B(Fe)-NH_2 electrodes, which were measured in solutions with different Cd^{2+} concentrations ranging from 25 nM to 1 μM. It can be observed from Fig. 6A that the peak current of the sensor increases when the Cd^{2+} concentration increases. Especially, the electrochemical signal is clearly observed even at a low Cd^{2+} concentration (25 nM). The increase in the Cd^{2+} concentration leads to an increase in the amount of Cd^{2+} ions accumulated on the electrode surface and an increase in the peak current. Fig. 6B gives a linear relationship between the peak current (I_{peak}) and the Cd^{2+} concentration (C^{2+}_{Cd}) in the range from 25 nM to 1 μM, which is I_{peak} (μA) = 0.0492 + 0.4492 × C^{2+}_{Cd} (μM) with a correlation coefficient of $R^2 = 0.9807$. Similarly, Fig. 6C shows DPV results performed in solutions with different Pb^{2+} concentrations ranging from 0.3 μM to 10 μM of the GCE/MIL-88B(Fe)-NH_2 electrodes. Fig. 6D depicts a linear relationship between the peak current (I_{peak}) and the Pb^{2+} concentration (C^{2+}_{Pb}) in the above range, which is I_{peak} (μA) = −0.0631 + 2.5642 × C^{2+}_{Pb} (μM) with a correlation coefficient of $R^2 = 0.9917$. Next, DPV results conducted in solutions with different Cu^{2+} concentrations ranging from 0.6 μM to 10 μM of the GCE/MIL-88B(Fe)-NH_2 electrodes are shown in Fig. 6E. A linear relationship between the peak current (I_{peak}) and the Cu^{2+} concentration (C^{2+}_{Cu}) in the above range, which is I_{peak} (μA) = −0.3810 + 1.0005 × C^{2+}_{Cu} (μM) with a correlation coefficient of $R^2 = 0.9871$, is given in Fig. 6F. The detection limit (LoD) of the developed electrochemical sensor for the Cd^{2+}, Pb^{2+} and Cu^{2+} ion detections were estimated at S/N > 3.[58,59] The obtained results revealed that using the GCE/MIL-88B(Fe)-NH_2 electrochemical sensors, the LoD can be obtained at 2.0 × 10^{-10} M for Cd^{2+}, 1.92 × 10^{-7} M for Pb^{2+} and 3.81 × 10^{-7} M for Cu^{2+}, respectively.

DPV results of the GCE/MIL-88B(Fe)-NH_2 electrode in solutions with simultaneous increments in all three ion concentrations (Cd^{2+}, Pb^{2+}, Cu^{2+}: from 2 μM to 10 μM) and their corresponding calibration plots are shown in Fig. 7A and B, respectively. These obtained results indicate that the fabricated sensor has a high reliability of developed chemical sensor. Moreover, the DPV results of the GCE/MIL-88B(Fe)-NH_2 electrodes in different solutions containing 5 μM Cd^{2+} + 5 μM Cu^{2+}, and Pb^{2+} with concentrations increasing from 2 μM to 10 μM, and the corresponding calibration plot of Pb^{2+} are depicted in

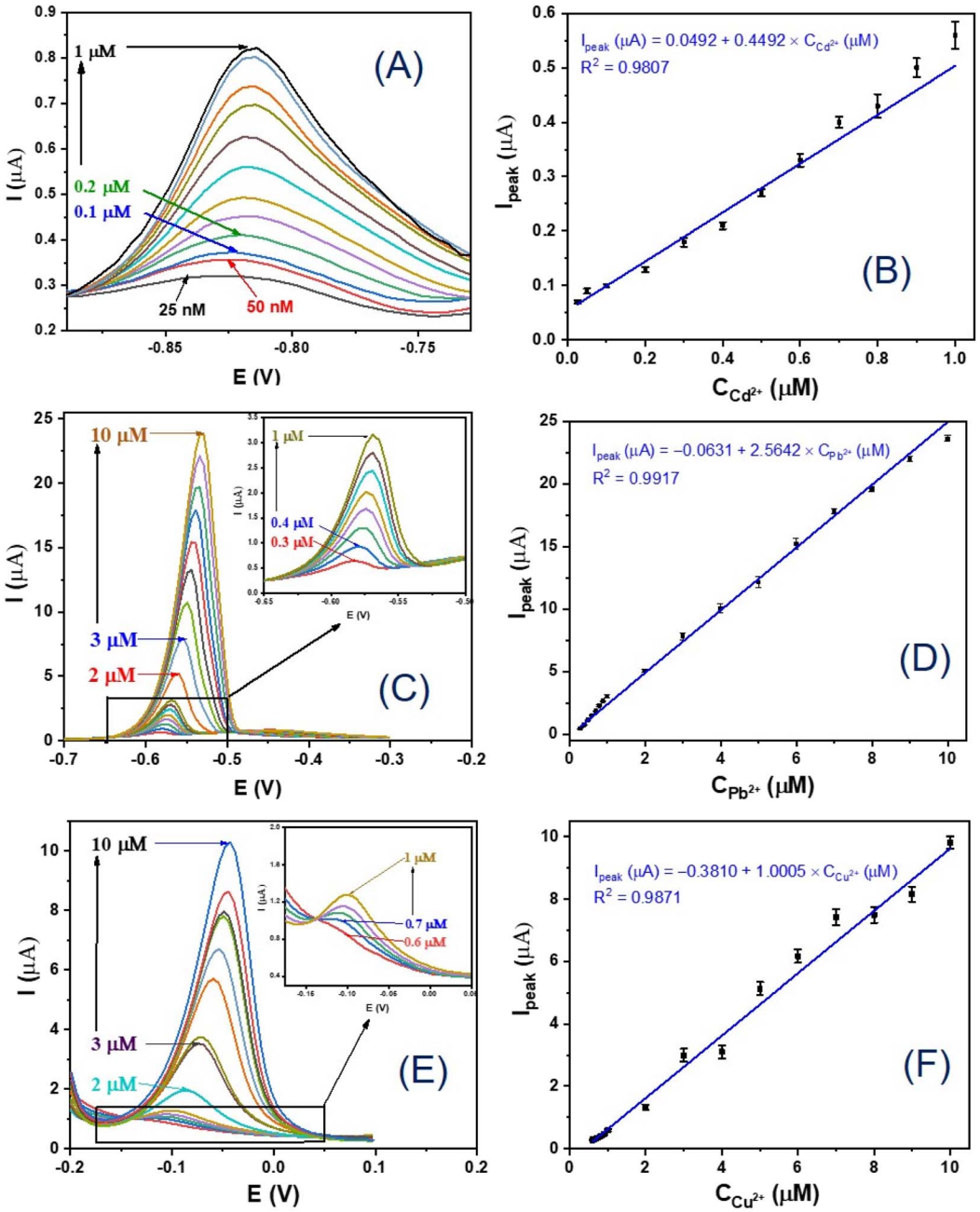

Fig. 6 (A, C and E) DPV results of GCE/MIL-88B(Fe)-NH_2 electrodes in 0.1 M ABS (pH = 6.0) solutions containing different concentrations of (A) Cd^{2+} (from 25 nM to 1 μM), (C) Pb^{2+} (from 0.3 μM to 10 μM) and (E) Cu^{2+} (from 0.6 μM to 10 μM); (B, D and F) The linear calibration curves exhibiting the relationship between the output signal of the electrochemical sensor and the concentration for (B) Cd^{2+}, (D) Pb^{2+}, and (F) Cu^{2+} ions, respectively.

Fig. 7C and D, in the order. Similarly, the DPV responses of the GCE/MIL-88B(Fe)-NH_2 electrodes in different solutions containing 5 μM Pb^{2+} + 5 μM Cu^{2+}, and Cd^{2+} with concentrations increasing from 2 μM to 10 μM, and the corresponding calibration plot of Cd^{2+} are exhibited in Fig. 2SA and B,† respectively. The DPV signals shown in Fig. 7C, D, 2SA and B† clearly demonstrate the ability of the obtained sensor to detect the ions in the desired ranges of detection. However, a point which is different from the single metal ion detection (Fig. 6A, C and E) is that a satellite peak appears on the right side of Pb^{2+} when three heavy metal ions are simultaneously detected (Fig. 7A and C). This satellite peak was demonstrated to be involved in the Pb–Cu interaction.[60,61] Moreover, the DPV results of GCE/MIL-88B(Fe)-NH_2 electrodes in solutions containing 10 μM Cd^{2+}, 10 μM Pb^{2+}, 10 μM Cu^{2+}, without and with other interfering ions, including Co^{2+}, Ni^{2+}, Zn^{2+}, $Cr_2O_7^{2-}$ (10 μM), and K^+, Cl^- (20 μM), which are provided in Fig. 8 (curve a and curve b, respectively), show that our electrochemical sensor has good selectivity.

When the fabricated sensor is used to detect the three heavy metal ions using the DPV method, firstly, Cd^{2+}, Pb^{2+} and Cu^{2+}

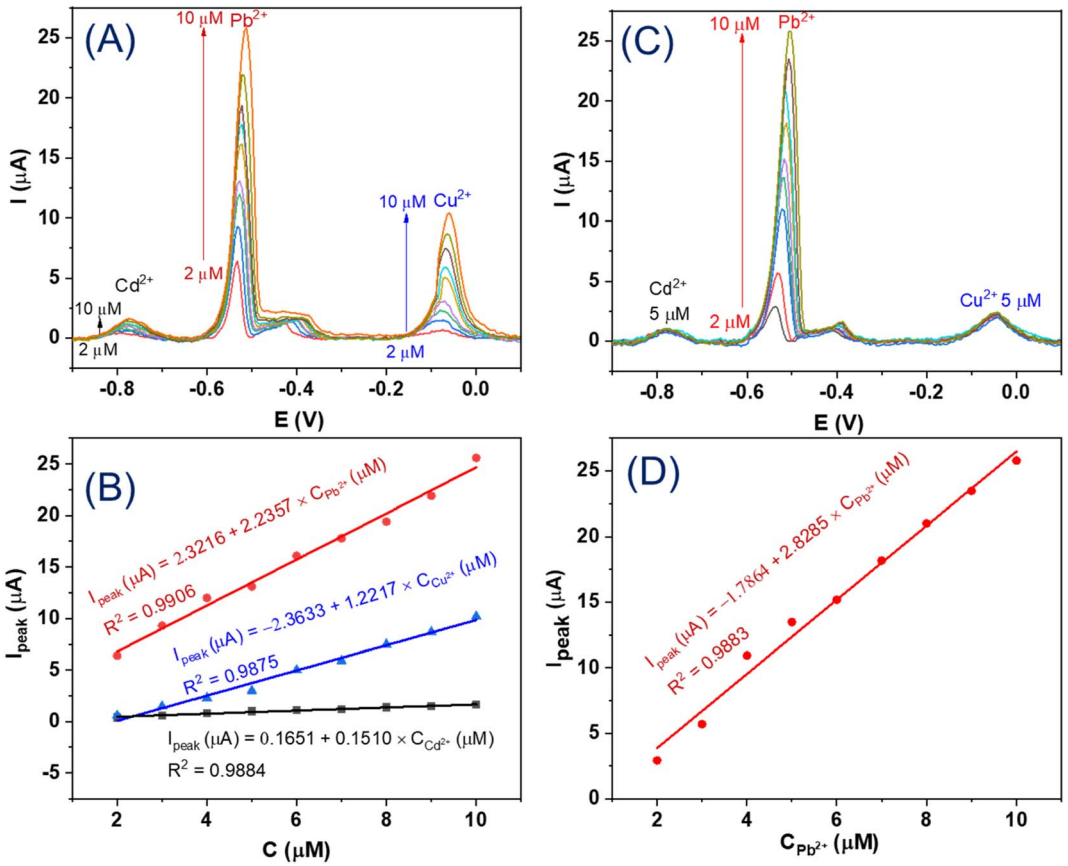

Fig. 7 (A) DPV response of the GCE/MIL-88B(Fe)-NH_2 electrode in 0.1 M ABS (pH = 6.0) solutions with simultaneous increments in all three ion concentrations (Cd^{2+}, Pb^{2+}, Cu^{2+}: from 2 μM to 10 μM), and (B) their corresponding calibration plots; (C) DPV results of GCE/MIL-88B(Fe)-NH_2 electrodes in 0.1 M ABS (pH = 6.0) solutions containing 5 μM Cd^{2+}, 5 μM Cu^{2+}, and Pb^{2+} with concentrations increasing from 2 μM to 10 μM, and (D) the linear relationship between the output signal of the sensor and the concentration of Pb^{2+}.

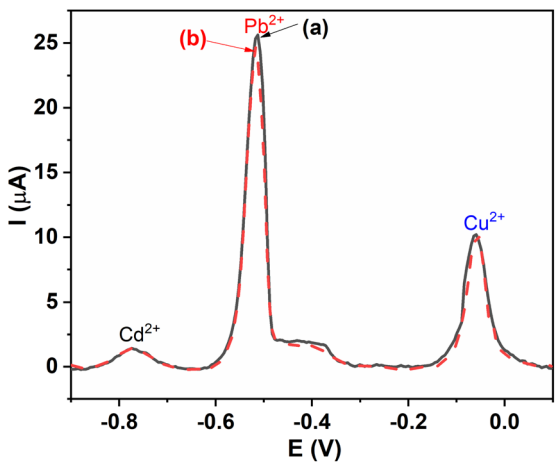

Fig. 8 DPV response of the GCE/MIL-88B(Fe)-NH_2 electrode in 0.1 M ABS (pH = 6.0) solutions containing 10 μM Cd^{2+}, 10 μM Pb^{2+}, 10 μM Cu^{2+}, (a) without (a black, solid line), and (b) with other interfering ions, including Co^{2+}, Ni^{2+}, Zn^{2+}, $Cr_2O_7^{2-}$: 10 μM, and K^+, Cl^-: 20 μM (a red, dashed line, each 40 μL of 5 mM solutions: $CoSO_4$, $NiSO_4$, $ZnCl_2$, and $K_2Cr_2O_7$ is added to the measuring system containing 20 mL of 0.1 M ABS (pH = 6.0) + 10 μM Cd^{2+} + 10 μM Pb^{2+} + 10 μM Cu^{2+}).

ions are adsorbed on the electrode surface and are reduced to form Cd, Pb, and Cu metals, respectively, during the deposition process with a constant negative potential applied (−1.2 V, 120 seconds, in this work); then, through the positive scan from a lower potential to a higher potential (from −0.9 to 0.1 V, in this study), these metals are oxidized, and the peak currents corresponding to their oxidation are recorded. The increase in the concentration of the heavy metal ions leads to the increase in the amount of the heavy metal ions adsorbed on the electrode surface, and the increase in the peak currents recorded after DPV measurements. The MIL-88B(Fe)-NH_2 layer with a large surface area has good adsorption capacity for Cd^{2+}, Pb^{2+}, and Cu^{2+} ions, so ion enrichments on the electrode surface are enhanced, and these ions can still be detected despite the low concentrations. Moreover, the electrocatalytic activity of the MIL-88B(Fe)-NH_2 material for the reduction of the metal ions is also an important reason for increasing the electrochemical signals. However, the adsorption capacity and electrocatalytic activity of MIL-88B(Fe)-NH_2 are different for different heavy metal ions, leading to the different limits of detection (2.0×10^{-10} M for Cd^{2+}, 1.92×10^{-7} M for Pb^{2+} and 3.81×10^{-7} M for Cu^{2+}, in this work). Moreover, an interesting characteristic is that Cd, Pb, and Cu metals are oxidized at the different

Table 2 Comparison of sensitivities and LODs of electrochemical sensors based on different materials for the detection of Cd^{2+}, Pb^{2+}, and Cu^{2+} ions

Electrode	Detection	Linear range (μM)	LOD (M)	Reference
GCE/NH_2-Fe_3O_4@C	Cd^{2+}	0.6–9.0	2.31×10^{-8}	50
	Pb^{2+}	1.2–10.0	2.85×10^{-8}	
	Cu^{2+}	0.4–4.0	3.84×10^{-8}	
GCE/MIL-53(Fe)	Cd^{2+}	0.15–0.45	1.6×10^{-8}	20
GCE/MIL-100(Cr)	Cd^{2+}	0–10	4.4×10^{-8}	51
	Pb^{2+}	0–10	4.8×10^{-8}	
	Cu^{2+}	0–10	1.1×10^{-8}	
GCE/Fe-OSA	Cd^{2+}	0.02–10.71	1.92×10^{-8}	52
	Pb^{2+}	0.04–13.40	3.6×10^{-8}	
	Cu^{2+}	0.15–15.45	8.78×10^{-8}	
GCE/BiONPs	Cd^{2+}	0.8–5.6	5×10^{-8}	53
	Pb^{2+}	0.4–2.8	1.5×10^{-7}	
GCE/Pd/PAC	Cd^{2+}	0.5–12.8	3.8×10^{-8}	54
	Pb^{2+}	0.5–22.4	2.5×10^{-8}	
	Cu^{2+}	0.5–11.8	1.3×10^{-7}	
GCE/CuNPs/rGO	Cd^{2+}	0.05–2.00	2.03×10^{-7}	55
	Pb^{2+}	0.05–3.00	1.86×10^{-7}	
	Cu^{2+}	0.05–2.50	1.11×10^{-7}	
GCE/Chitosan	Cd^{2+}	15.9–62.3	2.35×10^{-6}	56
	Pb^{2+}	1.99–15.80	3.09×10^{-7}	
	Cu^{2+}	3.99–39.10	8.99×10^{-7}	
GCE/Ni-MOF	Pb^{2+}	0.5–6.0	5.08×10^{-7}	57
GCE/MIL-88B(Fe)-NH_2	Cd^{2+}	0.025–1.000	2.0×10^{-10}	This study
	Pb^{2+}	0.3–10.0	1.92×10^{-7}	
	Cu^{2+}	0.6–10.0	3.81×10^{-7}	

potentials which characterize them (−0.79 V for Cd, −0.52 V for Pb, and −0.02 V for Cu, in our work). Therefore, the designed electrochemical sensor can be used to simultaneously detect the three heavy metal ions with high selectivity using DPV method.

As shown in Table 2, the fabricated GCE/MIL-88B(Fe)-NH_2 electrochemical sensor in this work is comparable to others summarized in previous works. In general, the MIL-88B(Fe)-NH_2-modified GCE possesses high sensitivity (especially in terms of Cd^{2+} detection), high reliability, and good selectivity. MIL-88B(Fe)-NH_2 is a promising MOF in the field of electrochemical sensors for detecting heavy metal ions, such as Cd^{2+}, Pb^{2+}, Cu^{2+}, and others.

4. Conclusion

The metal–organic framework MIL-88B(Fe)-NH_2 was synthesized *via* solvothermal method, and characterized by XRD, SEM, TEM, and FT-IR measurements. The impact of parameters on the material formation, including the molar ratio of $H_2NC_6H_3$-1,4-$(COOH)_2$/Fe(III) and the time reaction, was investigated in detail. Under the optimized experimental conditions, the sharpness and uniformity of the MIL-88B(Fe)-NH_2 crystals were obtained. The electrochemical sensor relying on the as-synthesized MIL-88B(Fe)-NH_2 indicates the brilliant result for the determination of Cd^{2+}, Pb^{2+} and Cu^{2+} with the low limit of detection, the wide linear detection range of concentrations, the high reliability, and the good selectivity. In addition, the fabrication method is simple and it can be extended for screen printing method for electrochemical sensor application in the disposal of heavy metal ions. Combining these above outcomes imply that MIL-88B(Fe)-NH_2 is capable of becoming a potential candidate applied as an electrochemical sensor for the detection of heavy metal ions in practice.

Conflicts of interest

There are no conflicts to declare.

Acknowledgements

This research was funded by the Vietnam Ministry of Education and Training (MOET) under grant number CT 2022.04.BKA.03.

References

1 S. Li and F. Huo, Metal-organic framework composites: from fundamentals to applications, *Nanoscale*, 2015, **7**, 7482–7501.
2 O. K. Farha, I. Eryazici, N. C. Jeong, B. G. Hauser, C. E. Wilmer, A. A. Sarjeant, *et al.*, Metal–Organic Framework Materials with Ultrahigh Surface Areas: Is the Sky the Limit?, *J. Am. Chem. Soc.*, 2012, **134**, 15016–15021.
3 X. Fang, B. Zong and S. Mao, Metal-Organic Framework-Based Sensors for Environmental Contaminant Sensing, *Nanomicro Lett.*, 2018, **10**, 64.
4 Y. Peng, V. Krungleviciute, I. Eryazici, J. T. Hupp, O. K. Farha and T. Yildirim, Methane Storage in Metal–Organic Frameworks: Current Records, Surprise Findings, and Challenges, *J. Am. Chem. Soc.*, 2013, **135**, 11887–11894.

5 T. M. McDonald, J. A. Mason, X. Kong, E. D. Bloch, D. Gygi, A. Dani, *et al.*, Cooperative insertion of CO2 in diamine-appended metal-organic frameworks, *Nature*, 2015, **519**, 303–308.

6 P. Horcajada, C. Serre, M. Vallet-Regí, M. Sebban, F. Taulelle and G. Férey, Metal–Organic Frameworks as Efficient Materials for Drug Delivery, *Angew. Chem., Int. Ed.*, 2006, **45**, 5974–5978.

7 A. R. Chowdhuri, D. Laha, S. Chandra, P. Karmakar and S. K. Sahu, Synthesis of multifunctional upconversion NMOFs for targeted antitumor drug delivery and imaging in triple negative breast cancer cells, *Chem. Eng. J.*, 2017, **319**, 200–211.

8 X. Cui, K. Chen, H. Xing, Q. Yang, R. Krishna, Z. Bao, *et al.*, Pore chemistry and size control in hybrid porous materials for acetylene capture from ethylene, *Science*, 2016, **353**, 141–144.

9 L. Meng, Q. Cheng, C. Kim, W.-Y. Gao, L. Wojtas, Y.-S. Chen, *et al.*, Crystal Engineering of a Microporous, Catalytically Active fcu Topology MOF Using a Custom-Designed Metalloporphyrin Linker, *Angew. Chem., Int. Ed.*, 2012, **51**, 10082–10085.

10 K. M. Park, H. Kim, J. Murray, J. Koo and K. Kim, A facile preparation method for nanosized MOFs as a multifunctional material for cellular imaging and drug delivery, *Supramol. Chem.*, 2017, **29**, 441–445.

11 Z. Hu, B. J. Deibert and J. Li, Luminescent metal–organic frameworks for chemical sensing and explosive detection, *Chem. Soc. Rev.*, 2014, **43**, 5815–5840.

12 X. Lian and B. Yan, Phosphonate MOFs Composite as Off–On Fluorescent Sensor for Detecting Purine Metabolite Uric Acid and Diagnosing Hyperuricuria, *Inorg. Chem.*, 2017, **56**, 6802–6808.

13 L. Cui, J. Wu, J. Li and H. Ju, Electrochemical Sensor for Lead Cation Sensitized with a DNA Functionalized Porphyrinic Metal–Organic Framework, *Anal. Chem.*, 2015, **87**, 10635–10641.

14 D. Duan, J. Ye, X. Cai and K. Li, Cobalt (II)-ion-exchanged Zn-bio-MOF-1 derived CoS/ZnS composites modified electrochemical sensor for chloroneb detection by differential pulse voltammetry, *Microchim. Acta*, 2021, **188**, 1–10.

15 P. Kumar, K.-H. Kim, P. K. Mehta, L. Ge and G. Lisak, Progress and challenges in electrochemical sensing of volatile organic compounds using metal-organic frameworks, *Crit. Rev. Environ. Sci. Technol.*, 2019, **49**, 2016–2048.

16 H. He, S.-Q. Wang, Z.-Y. Han, X.-H. Tian, W.-W. Zhang, C.-P. Li, *et al.*, Construction of electrochemical aptasensors with Ag (I) metal–organic frameworks toward high-efficient detection of ultra-trace penicillin, *Appl. Surf. Sci.*, 2020, **531**, 147342.

17 M. Chen, N. Gan, Y. Zhou, T. Li, Q. Xu, Y. Cao, *et al.*, An electrochemical aptasensor for multiplex antibiotics detection based on metal ions doped nanoscale MOFs as signal tracers and RecJf exonuclease-assisted targets recycling amplification, *Talanta*, 2016, **161**, 867–874.

18 J. Song, M. Huang, X. Lin, S. F. Y. Li, N. Jiang, Y. Liu, *et al.*, Novel Fe-based metal–organic framework (MOF) modified carbon nanofiber as a highly selective and sensitive electrochemical sensor for tetracycline detection, *Chem. Eng. J.*, 2022, **427**, 130913.

19 X. Fang, X. Chen, Y. Liu, Q. Li, Z. Zeng, T. Maiyalagan, *et al.*, Nanocomposites of Zr (IV)-based metal–organic frameworks and reduced graphene oxide for electrochemically sensing ciprofloxacin in water, *ACS Appl. Nano Mater.*, 2019, **2**, 2367–2376.

20 H. V. Tran, H. T. M. Dang, L. T. Tran, C. Van Tran and C. D. Huynh, Metal-Organic Framework MIL-53 (Fe): Synthesis, Electrochemical Characterization, and Application in Development of a Novel and Sensitive Electrochemical Sensor for Detection of Cadmium Ions in Aqueous Solutions, *Adv. Polym. Technol.*, 2020, **2020**, 6279278.

21 M. Ding, X. Cai and H.-L. Jiang, Improving MOF stability: approaches and applications, *Chem. Sci.*, 2019, **10**, 10209–10230.

22 S. Bauer, C. Serre, T. Devic, P. Horcajada, J. Marrot, G. Ferey, *et al.*, High-throughput assisted rationalization of the formation of metal organic frameworks in the iron (iii) aminoterephthalate solvothermal system, *Inorg. Chem.*, 2008, **47**, 7568–7576.

23 S. Yuan, L. Feng, K. Wang, J. Pang, M. Bosch, C. Lollar, *et al.*, Stable Metal-Organic Frameworks: Design, Synthesis, and Applications, *Adv. Mater.*, 2018, **30**, 1704303.

24 L. Paseta, B. Seoane, D. Julve, V. Sebastián, C. Téllez and J. Coronas, Accelerating the Controlled Synthesis of Metal–Organic Frameworks by a Microfluidic Approach: A Nanoliter Continuous Reactor, *ACS Appl. Mater. Interfaces*, 2013, **5**, 9405–9410.

25 T. Van Tran, D. T. C. Nguyen, H. T. Le, L. G. Bach, D.-V. N. Vo, T.-U. T. Dao, *et al.*, Effect of thermolysis condition on characteristics and nonsteroidal anti-inflammatory drugs (NSAIDs) absorbability of Fe-MIL-88B-derived mesoporous carbons, *J. Environ. Chem. Eng.*, 2019, **7**, 103356.

26 M. A. Yanuar and J. Kim, FeOF nanoparticles wrapped by graphitic carbon layers prepared from Fe-MIL-88B as a cathode material for sodium-ion batteries, *Carbon*, 2019, **149**, 483–491.

27 H. Zhang, S. Chen, H. Zhang, X. Fan, C. Gao, H. Yu, *et al.*, Carbon nanotubes-incorporated MIL-88B-Fe as highly efficient Fenton-like catalyst for degradation of organic pollutants, *Front. Environ. Sci. Eng.*, 2019, **13**, 18.

28 Y. Wang, Z. Zhong, Y. Muhammad, H. He, Z. Zhao, S. Nie, *et al.*, Defect engineering of NH_2-MIL-88B (Fe) using different monodentate ligands for enhancement of photo-Fenton catalytic performance of acetamiprid degradation, *Chem. Eng. J.*, 2020, **398**, 125684.

29 X. Liao, F. Wang, Y. Wang, W. Wei, Z. Xiao, H. Liu, *et al.*, Functionalized g-C3N4 sheets assisted synthesis of growth-oriented MIL-88B-Fe with rod-like structure: Upgrading framework photo-catalytic performance and stability, *Appl. Surf. Sci.*, 2020, **503**, 144089.

30 M. P. Waalkes, Cadmium carcinogenesis in review, *J. Inorg. Biochem.*, 2000, **79**, 241–244.
31 M. Boskabady, N. Marefati, T. Farkhondeh, F. Shakeri, A. Farshbaf and M. H. Boskabady, The effect of environmental lead exposure on human health and the contribution of inflammatory mechanisms, a review, *Environ. Int.*, 2018, **120**, 404–420.
32 M. Angelova, S. Asenova, V. Nedkova and R. Koleva-Kolarova, Copper in the human organism, *Trakia J. Sci.*, 2011, **9**, 88–98.
33 X. Y. Xu and B. Yan, Intelligent molecular searcher from logic computing network based on Eu(III) functionalized UMOFs for environmental monitoring, *Adv. Funct. Mater.*, 2017, **27**, 1700247.
34 J. Hao, F. Liu, N. Liu, M. Zeng, Y. Song and L. Wang, Ratiometric fluorescent detection of Cu^{2+} with carbon dots chelated Eu-based metal-organic frameworks, *Sens. Actuators, B*, 2017, **245**, 641–647.
35 Y. Wang, Y. Wu, J. Xie and X. Hu, Metal–organic framework modified carbon paste electrode for lead sensor, *Sens. Actuators, B*, 2013, **177**, 1161–1166.
36 J.-C. Jin, J. Wu, G.-P. Yang, Y.-L. Wu and Y.-Y. Wang, A microporous anionic metal–organic framework for a highly selective and sensitive electrochemical sensor of Cu 2+ ions, *Chem. Commun.*, 2016, **52**, 8475–8478.
37 S. E. A. Elashery, N. F. Attia and H. Oh, Design and fabrication of novel flexible sensor based on 2D Ni-MOF nanosheets as a preliminary step toward wearable sensor for onsite Ni (II) ions detection in biological and environmental samples, *Anal. Chim. Acta*, 2022, **1197**, 339518.
38 S. E. A. Elashery and H. Oh, Exploitation of 2D Cu-MOF nanosheets as a unique electroactive material for ultrasensitive Cu(II) ion estimation in various real samples, *Anal. Chim. Acta*, 2021, **1181**, 338924.
39 M. E. B. Mohamed, N. F. Attia and S. E. A. Elashery, Greener and facile synthesis of hybrid nanocomposite for ultrasensitive iron (II) detection using carbon sensor, *Microporous Mesoporous Mater.*, 2021, **313**, 110832.
40 E. Y. Frag, N. M. Mohamed and S. E. A. Elashery, Exploitation of o-benzoyl benzoic acid as an efficient electroactive material for selective determination of Cr (III) ions in pharmaceutical samples and industrial waste water using carbon sensor, *Anal. Chim. Acta*, 2021, **1154**, 338322.
41 E. Aghaei and M. Haghighi, Effect of crystallization time on properties and catalytic performance of nanostructured SAPO-34 molecular sieve synthesized at high temperatures for conversion of methanol to light olefins, *Powder Technol.*, 2015, **269**, 358–370.
42 N. Al-Janabi, P. Hill, L. Torrente-Murciano, A. Garforth, P. Gorgojo, F. Siperstein, *et al.*, Mapping the Cu-BTC metal–organic framework (HKUST-1) stability envelope in the presence of water vapour for CO_2 adsorption from flue gases, *Chem. Eng. J.*, 2015, **281**, 669–677.
43 X. Li, J. Zhang, W. Shen and S. Xu, Rapid synthesis of metal-organic frameworks MIL-53 (Cr), *Mater. Lett.*, 2019, **255**, 126519.
44 X. Li, W. Guo, Z. Liu, R. Wang and H. Liu, Fe-based MOFs for efficient adsorption and degradation of acid orange 7 in aqueous solution *via* persulfate activation, *Appl. Surf. Sci.*, 2016, **369**, 130–136.
45 L. Wang, S. Duan, M. Fang, J. Liu, J. He, J. Li, *et al.*, Surface modification route to prepare novel polyamide@NH2 MIL-88B nanocomposite membranes for water treatment, *RSC Adv.*, 2016, **6**, 71250–71261.
46 Y. L. Liu, X. J. Zhao, X. X. Yang and Y. F. Li, A nanosized metal–organic framework of Fe-MIL-88NH2 as a novel peroxidase mimic used for colorimetric detection of glucos, *Analyst*, 2013, **138**, 4526–4531.
47 M.-H. Pham, G.-T. Vuong, A.-T. Vu and T.-O. Do, Novel Route to Size-Controlled Fe–MIL-88B–NH_2 Metal–Organic Framework Nanocrystals, *Langmuir*, 2011, **27**, 15261–15267.
48 Y. Li, J. Jiang, Y. Fang, Z. Cao, D. Chen, N. Li, *et al.*, TiO2 Nanoparticles Anchored onto the Metal-Organic Framework NH2-MIL-88B(Fe) as an Adsorptive Photocatalyst with Enhanced Fenton-like Degradation of Organic Pollutants under Visible Light Irradiation, *ACS Sustainable Chem. Eng.*, 2018, **6**, 16186–16197.
49 H. Sun, C. Wang, Y. Xu, D. Dai, X. Deng and H. Gao, A Novel Electrochemical Sensor Based on A Glassy Carbon Electrode Modified with GO/MnO for Simultaneous Determination of Trace Cu(II) and Pb(II) in Environmental Water, *ChemistrySelect*, 2019, **4**, 11862–11871.
50 F. Bai, X. Zhang, X. Hou, H. Liu, J. Chen and T. Yang, Individual and simultaneous voltammetric determination of Cd (II), Cu (II) and Pb (II) applying amino functionalized Fe_3O_4@ carbon microspheres modified electrode, *Electroanalysis*, 2019, **31**, 1448–1457.
51 D. Wang, Y. Ke, D. Guo, H. Guo, J. Chen and W. Weng, Facile fabrication of cauliflower-like MIL-100(Cr) and its simultaneous determination of Cd^{2+}, Pb^{2+}, Cu^{2+} and Hg^{2+} from aqueous solution, *Sens. Actuators, B*, 2015, **216**, 504–510.
52 H. Sha, Y. Wu and Y. Fan, A Fe-OSA/Nafion composite film-decorated glassy carbon electrode as a sensor for detection of Pb (II), Cd (II) and Cu (II), *Anal. Methods*, 2017, **9**, 5618–5631.
53 C. Hao, Y. Shen, J. Shen, K. Xu, X. Wang, Y. Zhao, *et al.*, A glassy carbon electrode modified with bismuth oxide nanoparticles and chitosan as a sensor for Pb (II) and Cd (II), *Microchim. Acta*, 2016, **183**, 1823–1830.
54 P. Veerakumar, V. Veeramani, S. M. Chen, R. Madhu and S. B. Liu, Palladium nanoparticle incorporated porous activated carbon: electrochemical detection of toxic metal ions, *ACS Appl. Mater. Interfaces*, 2016, **8**, 1319–1326.
55 D. Li, C. Wang, H. Zhang, Y. Sun, Q. Duan, J. Ji, *et al.*, A highly effective copper nanoparticle coupled with RGO for electrochemical detection of heavy metal ions, *Int. J. Electrochem. Sci.*, 2017, **12**, 10933–10945.
56 C. Martínez-Huitle, N. S. Fernandes, M. Cerro-Lopez and M. Quiroz, Determination of trace metals by differential pulse voltammetry at chitosan modified electrodes, *Port. Electrochim. Acta*, 2010, **28**, 39–49.

57 H. Guo, Z. Zheng, Y. Zhang, H. Lin and Q. Xu, Highly selective detection of Pb^{2+} by a nanoscale Ni-based metal–organic framework fabricated through one-pot hydrothermal reaction, *Sens. Actuators, B*, 2017, **248**, 430–436.

58 H. V. Tran, B. Piro, S. Reisberg, L. D. Tran, H. T. Duc and M. C. Pham, Label-free and reagentless electrochemical detection of microRNAs using a conducting polymer nanostructured by carbon nanotubes: application to prostate cancer biomarker miR-141, *Biosens. Bioelectron.*, 2013, **49**, 164–169.

59 H. V. Tran, C. D. Huynh, T. D. Le and H. S. Hoang, Hydroxyapatite Nano-Rods/Chitosan Modified Glassy Carbon Electrode for Cu(II) Ions Determination, *Electron. Mater. Lett.*, 2020, **16**, 396–403.

60 Z. Tan, W. Wu, C. Feng, H. Wu and Z. Zhang, Simultaneous determination of heavy metals by an electrochemical method based on a nanocomposite consisting of fluorinated graphene and gold nanocage, *Mikrochim. Acta*, 2020, **187**, 414.

61 Z. Zhai, N. Huang, H. Zhuang, L. Liu, B. Yang, C. Wang, *et al.*, A diamond/graphite nanoplatelets electrode for anodic stripping voltammetric trace determination of Zn(II), Cd(II), Pb(II) and Cu(II), *Appl. Surf. Sci.*, 2018, **457**, 1192–1201.